Kinematics of nonlinear waves over variable bathymetry. Part I: Numerical modelling, verification and validation

Michel Benoit, Jie Zhang, Yuxiang Ma

Kinematics of nonlinear waves over variable bathymetry. Part I: Numerical modelling, verification and validation

Michel Benoit[a,b], Jie Zhang[c,d,*] and Yuxiang Ma[e]

[a]EDF R&D, Laboratoire National d'Hydraulique et Environnement (LNHE), Chatou, France
[b]LHSV, Saint-Venant Hydraulics Laboratory (Ecole des Ponts, EDF R&D), Chatou, France
[c]Qingdao Innovation and Development Base, Harbin Engineering University, Qingdao 266400, PR China
[d]Qingdao Innovation and Development Center of Harbin Engineering University, Qingdao 266400, PR China
[e]State Key Laboratory of Coastal and Offshore Engineering, Dalian University of Technology, Dalian 116023, PR China

ARTICLE INFO

Keywords:
Coastal waves
Nonlinear waves
Wave kinematics
Numerical simulation
Statistical parameters

ABSTRACT

Fluid particle kinematics due to wave motion (i.e. orbital velocities and accelerations) at and beneath the free surface is involved in many coastal and ocean engineering applications, e.g. estimation of wave-induced forces on structures, sediment transport, etc. This work presents the formulations of these kinematics fields within a fully nonlinear potential flow (FNPF) approach. In this model, the velocity potential is approximated with a high-order polynomial expansion over the water column using an orthogonal basis of Chebyshev polynomials of the first kind. Using the same basis, original analytical expressions of the components of velocity and acceleration are derived in this work. The estimation of particle accelerations in the course of the simulation involves the time derivatives of the decomposition coefficients, which are computed with a high-order backward finite-difference scheme in time. The capability of the numerical model in computing the particle kinematics is first validated for regular nonlinear waves propagating over a flat bottom. The model is shown to be able to predict both the velocity and acceleration of highly nonlinear and nearly breaking waves with negligible error compared to the corresponding stream function wave solution. Then, for regular waves propagating over an uneven bottom (bar-type bottom profile), the simulated results are confronted with existing experimental data, and very good agreement is achieved up to the sixth-order harmonics for free surface elevation, velocity and acceleration.

1. Introduction

Water wave kinematics has been studied for decades because it is of core importance in the design procedures of coastal and harbour engineering (e.g. Fredsøe and Deigaard, 1992). The distribution of total pressure, water particle velocities and accelerations plays a fundamental role when evaluating forces on marine structures, the motion of sediments and the evolution of coastal morphology (Freilich and Guza, 1984; Kriebel, 1998; Elfrink and Baldock, 2002; Wilson, 2002). Under the background of global warming, coastal and harbour engineering is faced with more frequent and disruptive extreme events (see e.g. Didenkulova and Pelinovsky, 2016, 2020; Didenkulova et al., 2023; Shi et al., 2024). To balance safety and economy, a better understanding and prediction of the flow field beneath strongly nonlinear waves remains of paramount importance (Zelt et al., 1995; Stansberg et al., 1995; Aggarwal et al., 2016; Vested et al., 2020; Li et al., 2023; Deng et al., 2023).

To obtain the spatial and temporal evolution of wave kinematics, deterministic (phase-resolving) models are needed. The Computational Fluid Dynamics (CFD) approach solves the Navier–Stokes equations which account for nonlinearity, vorticity and viscosity. It is very powerful in describing the flow of fluids, and in offering the pressure and velocity profiles. The Reynolds Averaged Navier–Stokes (RANS) equations, solved with either Lagrangian (Dalrymple and Rogers, 2006; Antuono et al., 2011) or Eulerian (Wang et al., 2009; Higuera et al., 2013; Jacobsen et al., 2015) methods, are often used in the studies of wave breaking, wave-structure interactions, and multiphase flows. One drawback of RANS equations is the high computational burden, limiting the spatial and temporal scale of the simulations. In addition, as shown recently by Larsen et al. (2019) for instance, the accuracy of computed wave kinematics is not always guaranteed with this kind of code, in particular in the vicinity of the free surface, depending on the employed numerical methods and the discretization parameters selected to solve this set of equations numerically.

Besides, there are very efficient yet simplified wave models with assumptions on the magnitudes of wave steepness and/or relative water depth, namely the weakly nonlinear and dispersive models. For instance, mild slope equation, Boussinesq equation, nonlinear Schrödinger equation, Serre-Green-Naghdi equation belong to this class (Berkhoff, 1972; Porter, 2003; Boussinesq, 1872; Madsen and Schäffer, 1998; Hasimoto and Ono, 1972; Dysthe, 1979; Green et al., 1974; Bassi et al., 2020, just to name a few in these topics). As the name indicates, models of this type are developed for handling weakly nonlinear and dispersive wave cases, i.e. in the long-wave regime. Therefore, they assume simplified representations of the profiles of horizontal and vertical velocity components in the vertical direction, typically using low-order polynomial expressions (i.e. linear or quadratic). Al-

*Corresponding author
michel.benoit@edf.fr (M. Benoit); jie.zhang@hrbeu.edu.cn (J. Zhang); yuxma@dlut.edu.cn (Y. Ma)
ORCID(s): 0000-0003-4195-2983 (M. Benoit); 0000-0003-0794-2335 (J. Zhang); 0000-0003-4314-0428 (Y. Ma)

though there are numerous extensions of the above-mentioned models, all being able to include higher-order effects, they often end up in cumbersome mathematical expressions with high-order derivatives which are tricky for numerical implementation.

As a compromise between efficiency and accuracy, given the viscous and turbulent effects are often negligible for wave propagation studies, the fully nonlinear potential flow (FNPF) model represents a powerful tool for wave modelling in a range of dozens of wavelengths. In recent years, it has received considerable attention and undergone substantial progress. On the one hand, this mathematical model makes no a priori assumption about the magnitude of wave steepness and relative water depth, thus it is capable of describing all nonlinear features of non-overturning waves. On the other hand, it is convenient to compute the particle velocity and acceleration from the scalar velocity potential. Besides, it can be used to provide input wave fields and to couple with CFD models (Paulsen et al., 2014; Decorte et al., 2021). The FNPF model can be solved with the Boundary Element Method (BEM) that projects the problem on the boundary surface of the fluid domain using Green's identity and function (Grilli et al., 1989; Fochesato and Dias, 2006; Harris et al., 2014) or with the so-called using "Zakharov formulation" that formulates the problem with free surface variables (Zakharov, 1968; Craig and Sulem, 1993), both methods allowing for a reduction of the dimension of the computational problem. Among many approaches, the High-Order Spectral method (Dommermuth, 2000; Gouin et al., 2016; Lawrence et al., 2021a), high-order Boussinesq-type models (Madsen et al., 2006; Bingham et al., 2009) and the Hamiltonian couple-mode theory (Belibassakis and Athanassoulis, 2011; Papoutsellis et al., 2019) have been used to solve the Zakharov formulation of the FNPF model. Recently, a numerical solver of the Zakharov formulation has been developed using a highly accurate approximation of the velocity potential through the use of a spectral approach in the vertical direction with a set of orthogonal polynomials (Tian and Sato, 2008; Yates and Benoit, 2015; Raoult et al., 2016; Benoit et al., 2017). The resulting computational code, called Whispers3D (abbreviated W3D hereafter), shows excellent accuracy in predicting the evolution of highly nonlinear free surface waves over steep slopes (Zhang and Benoit, 2021; Zhang et al., 2022). The W3D code is also capable of handling wave breaking with various options for breaking initiation criteria and dissipation mechanisms (Simon et al., 2019). However, the capability of this model in describing wave kinematics at and beneath the free surface elevation (FSE) has not been discussed yet, except partially in the work of Zhang and Benoit (2021). In the present work, W3D performance in calculating the velocity and acceleration directly and explicitly is thoroughly examined, namely by first deriving analytical expressions of these kinematic fields, and then applying these new results to compute velocity and acceleration fields for highly nonlinear waves over flat and uneven bottoms.

The remainder of this article is organized as follows: in section 2, the computation formulas of particle velocity and acceleration are derived within the model formulation; section 3 presents the verification of the method for highly nonlinear regular waves case propagating in uniform water depth against analytical results computed with the exact stream function (SF) theory; section 4 shows the experimental validation for a nonlinear regular wave shoaling and de-shoaling case over a submerged trapezoidal bar, the simulation results are compared with measurements in both spectral and statistical domain.Conclusions are provided in section 5.

2. Mathematical wave model and internal kinematics

2.1. Overview of the wave model

Within the framework of potential theory, assuming that (i) the fluid is inviscid and incompressible, (ii) the flow is irrotational, and (iii) the waves are non-breaking, the fluid motion can be described by the velocity potential ϕ. In addition, the free surface tension is neglected here, for simplicity. The above assumptions do not imply any restriction on the magnitude of the wave steepness nor on the relative water depth, thus the full nonlinearity and dispersion of waves are retained. Consider a two-dimensional case in a Cartesian coordinate system (x, z), with z-axis pointing upward and $z = 0$ located at the still water level (SWL), the governing equations of the FNPF theory are:

$$\Delta\phi = 0 \quad \text{for } z \in [-h,\, \eta], \tag{1}$$

$$\eta_t + \phi_x\eta_x - \phi_z = 0 \quad \text{on } z = \eta, \tag{2}$$

$$\phi_t + \frac{1}{2}\left(\phi_x^2 + \phi_z^2\right) + g\eta = 0 \quad \text{on } z = \eta, \tag{3}$$

$$h_x\phi_x + \phi_z = 0 \quad \text{on } z = -h, \tag{4}$$

where Δ denotes the Laplace operator, $\eta(x,t)$ denotes the FSE, $h(x)$ the water depth, and g the acceleration due to gravity. Partial derivatives are denoted with subscripts (e.g. $\eta_x \equiv \partial\eta/\partial x$).

Following Zakharov (1968) and Craig and Sulem (1993), the FNPF problem can be reformulated as a functional of two free surface variables, i.e., the FSE $\eta(x,t)$ and the free surface potential $\tilde{\phi}(x,t) \equiv \phi(x, z = \eta, t)$. The reformulation allows describing the motion of the bulk fluid by rewriting the nonlinear free surface boundary conditions (2) and (3) as:

$$\eta_t = -\tilde{\phi}_x\eta_x + \tilde{w}\left[1 + \left(\eta_x\right)^2\right], \tag{5}$$

$$\tilde{\phi}_t = -g\eta - \frac{1}{2}\left(\tilde{\phi}_x\right)^2 + \frac{1}{2}\tilde{w}^2\left[1 + \left(\eta_x\right)^2\right], \tag{6}$$

where $\tilde{w}(x,t) \equiv \phi_z(x, z = \eta, t)$ denotes the vertical velocity of the water particles on the free surface. Partial derivatives of $\tilde{\phi}$ are deduced via the chain rule. The two coupled equations (5–6) describe the change rate of $\tilde{\phi}$ and η in time, with $\tilde{w}$ being the only unknown variable. Solving $\tilde{w}$ from the boundary conditions $(\eta, \tilde{\phi})$ on the free surface is the so-called *Dirichlet-to-Neumann* (DtN) problem. The DtN problem is of fundamental importance for the Zakharov

formulation and has been extensively studied. For a more detailed introduction of various approaches for solving the DtN problem in different models and the methodology adopted in W3D, the readers are referred to Tian and Sato (2008); Yates and Benoit (2015); Raoult et al. (2016), and the references therein. Here, we first briefly review the key steps of solving the DtN problem in W3D, then introduce the calculation of internal kinematics in this model.

First, the physical (x, z) domain with variable boundaries in the vertical direction $z \in [-h(x), \eta(x,t)]$ is mapped to a new (x, s) domain with fixed boundaries $s \in [-1, 1]$ via the transformation of vertical coordinate:

$$s(x,z,t) = \frac{2z + h^-(x,t)}{h^+(x,t)} \tag{7}$$

with $h^\pm(x,t) \equiv h(x) \pm \eta(x,t)$. The potential is expressed as $\varphi(x, s(x,z,t), t) \equiv \phi(x,z,t)$ in the transformed domain, in which the governing equations are reformulated (not shown here, see e.g. (Yates and Benoit, 2015)).

Then, the velocity potential is projected onto an orthogonal polynomial basis formed by the set of Chebyshev polynomials of the first kind, denoted $T_n(s)$, up to a maximal order denoted N_T. The potential φ is approximated as:

$$\varphi(x,s,t) \approx \varphi_{N_T}(x,s,t) = \sum_{n=0}^{N_T} a_n(x,t) T_n(s), \tag{8}$$

where the coefficients $a_n(x,t), n = 0, 1, ..., N_T$, are the $N_T + 1$ unknowns of the problem (at each abscissa x). The N_T parameter plays a central role in balancing model accuracy and computational effort. Benoit et al. (2017) showed the capability of the linearized W3D model in describing the linear dispersion, which serves as a good starting point in calibrating the value of N_T. Usually, for waves with intermediate nonlinearity propagating in finite water depth, choosing $N_T = 7$ yields already very accurate predictions. We may need to tune N_T for higher values when considering highly nonlinear waves (close to breaking) or very deep water conditions ($\mu \sim 10$). Inserting eq. (8) into the Laplace equation and adopting the Chebyshev-tau method to remove the dependency on the s variable, $N_T - 1$ linear equations are built. With two supplementary equations drawn from the free surface and bottom boundary conditions, the problem is closed with $N_T + 1$ linear equations for $N_T + 1$ unknowns.

Then, $\tilde{w}$ can be evaluated as:

$$\tilde{w}(x,t) = \frac{2}{h^+(x,t)} \sum_{n=1}^{N_T} a_n(x,t) n^2. \tag{9}$$

The DtN problem is thus solved and, with $\tilde{w}$ known, eqs. (5–6) can be stepped forward in time. Several time marching schemes are implemented in W3D. Here we used the explicit third-order strong stability preserving Runge-Kutta scheme with a constant time-step Δt. Unless otherwise stated, all first- and second-order x-derivatives in the numerical model are approximated with finite difference (FD) formulas using a centered stencil of $N_{sten} = 5$ nodes, which provides fourth-order formal accuracy in the case of uniform grid size Δx.

2.2. Computation of orbital velocities

With the a_n coefficients determined, the orbital velocities can be evaluated at any point in the fluid domain by taking the spatial derivatives of $\phi(x,z,t)$. To that end, we first give the expressions of the partial derivatives of the vertical coordinate $s(x,z,t)$, obtained from eq. (7), as:

$$s_x = \frac{h_x^- - s h_x^+}{h^+} = \frac{h_x}{h^+}(1-s) - \frac{\eta_x}{h^+}(1+s), \tag{10}$$

$$s_z = \frac{2}{h^+}, \tag{11}$$

$$s_t = \frac{h_t^- - s h_t^+}{h^+} = -\frac{\eta_t}{h^+}(1+s), \tag{12}$$

$$s_{xt} = -\frac{1}{h^+}\left[\eta_{xt}(1+s) + \eta_t s_x + s_t h_x^+\right], \tag{13}$$

$$s_{zt} = -\frac{2\eta_t}{(h^+)^2}. \tag{14}$$

The horizontal velocity $u(x,z,t) = \phi_x$ and the vertical velocity $w(x,z,t) = \phi_z$ are expressed as functions of the a_n coefficients and their x-derivatives:

$$\begin{aligned} u(x,z,t) &\approx \frac{\partial \varphi_{N_T}}{\partial x} + s_x \frac{\partial \varphi_{N_T}}{\partial s} \\ &= \sum_{n=0}^{N_T} a_{n,x} T_n + \frac{h_x^- - s h_x^+}{h^+} \sum_{n=1}^{N_T} a_n T_{n,s}, \end{aligned} \tag{15}$$

$$w(x,z,t) \approx s_z \frac{\partial \varphi_{N_T}}{\partial s} = \frac{2}{h^+} \sum_{n=1}^{N_T} a_n T_{n,s}. \tag{16}$$

These expressions can be projected on the basis formed by the orthogonal polynomials $\{T_n, n = 0, ..., N_T\}$ using the inner product defined in Eq. (24) of Raoult et al. (2019), and equivalently reformulated in a compact form, as:

$$u(x,z,t) = \sum_{p=0}^{N_T} a_p^u T_p, \tag{17}$$

$$w(x,z,t) = \sum_{p=0}^{N_T - 1} a_p^w T_p, \tag{18}$$

with the coefficients $a_p^u, p = 0, ..., N_T$, and $a_p^w, p = 0, ..., N_T - 1$, given analytically by:

$$a_p^u = a_{p,x} + \frac{1}{h^+}(h_x^- S_{1p} - h_x^+ S_{2p}), \tag{19}$$

$$a_p^w = \frac{2}{h^+} S_{1p}. \tag{20}$$

where

$$S_{1p} \equiv \sum_{n=1}^{N_T} a_n B_{p01n}, \tag{21}$$

$$S_{2p} \equiv \sum_{n=1}^{N_T} a_n B_{p11n}. \tag{22}$$

The expressions of the terms B_{p01n} and B_{p11n} are already defined in appendix B of Raoult et al. (2019), thus not repeated here for brevity. We note the maximum degree of T_n polynomials is N_T for u in eq. (17) and $N_T - 1$ for w in eq. (18).

2.3. Computation of Eulerian accelerations

The local (Eulerian) accelerations $ax(x,z,t) = u_t$ and $az(x,z,t) = w_t$ are obtained as:

$$ax \approx \sum_{n=0}^{N_T} a_{n,xt} T_n + \sum_{n=1}^{N_T} \left[s_t a_{n,x} + s_{xt} a_n + s_x a_{n,t} \right] T_{n,s} + s_x s_t \sum_{n=2}^{N_T} a_n T_{n,ss}, \tag{23}$$

$$az \approx \sum_{n=1}^{N_T} (s_z a_{n,t} + s_{zt} a_n) T_{n,s} + s_z s_t \sum_{n=2}^{N_T} a_n T_{n,ss} \tag{24}$$

As for the velocity components, these expressions can be projected on the basis $\{T_n, n = 0, ..., N_T\}$ and equivalently reformulated as:

$$ax(x,z,t) = \sum_{p=0}^{N_T} a_p^{ax} T_p, \tag{25}$$

$$az(x,z,t) = \sum_{p=0}^{N_T-1} a_p^{az} T_p, \tag{26}$$

with the coefficients a_p^{ax}, $p = 0, ..., N_T$, and a_p^{az}, $p = 0, ..., N_T - 1$, given analytically by:

$$a_p^{ax} = a_{p,xt} - \frac{2}{h^+} \left[\eta_t (S_{3p} + S_{4p}) + (\eta_{xt} - 2\frac{\eta_t \eta_x}{h^+}) \times (S_{1p} + S_{2p}) - 2\frac{\eta_t h_x}{h^+} S_{2p} - h_x^- S_{5p} + h_x^+ S_{6p} \right] + \frac{\eta_t}{(h^+)^2} \left[h_x (S_{9p} - S_{7p}) + \eta_x (S_{7p} + 2S_{8p} + S_{9p}) \right], \tag{27}$$

$$a_p^{az} = \frac{2}{h^+} \left(S_{5p} - \frac{\eta_t}{h^+} \left(S_{1p} + S_{7p} + S_{8p} \right) \right), \tag{28}$$

where

$$S_{3p} \equiv \sum_{n=1}^{N_T} a_{n,x} B_{p01n} = \frac{\partial S_{1p}}{\partial x}, \tag{29}$$

$$S_{4p} \equiv \sum_{n=1}^{N_T} a_{n,x} B_{p11n} = \frac{\partial S_{2p}}{\partial x}, \tag{30}$$

$$S_{5p} \equiv \sum_{n=1}^{N_T} a_{n,t} B_{p01n} = \frac{\partial S_{1p}}{\partial t}, \tag{31}$$

$$S_{6p} \equiv \sum_{n=1}^{N_T} a_{n,t} B_{p11n} = \frac{\partial S_{2p}}{\partial t}, \tag{32}$$

$$S_{7p} \equiv \sum_{n=1}^{N_T} a_n B_{p02n}, \tag{33}$$

$$S_{8p} \equiv \sum_{n=1}^{N_T} a_n B_{p12n}, \tag{34}$$

$$S_{9p} \equiv \sum_{n=1}^{N_T} a_{n,t} B_{p22n}. \tag{35}$$

The expressions of the terms B_{p02n}, B_{p12n} and B_{p22n} are also provided in Raoult et al. (2019).

To compute the accelerations, we need to provide the time derivatives of the FSE, denoted η_t (appearing in eqs. (12)–(14)), and those of the a_n coefficients, denoted $a_{n,t}$ (appearing in eqs. (23)–(24)). For η_t, we use the expression at the right-hand side of eq. (5). Then, η_{xt} can be obtained from η_t with the 5-node centered FD scheme mentioned above.

The $a_{n,t}$ terms are computed using a high-order FD scheme in time, with two options available:

- calculation of kinematics after completion of the simulation: a centered scheme around the current time instant is used, with again a 5-node stencil:

$$a_{n,t}(t) = \frac{1}{12\Delta t} \left[8 \left(a_n(t + \Delta t) - a_n(t - \Delta t) \right) - \left(a_n(t + 2\Delta t) - a_n(t - 2\Delta t) \right) \right] \tag{36}$$

- calculation in the course of the simulation: an upwind scheme is used, with the current value of a_n and the three previous ones (giving third-order formal accuracy):

$$a_{n,t}(t) = \frac{1}{\Delta t} \left[\frac{11}{6} a_n(t) - 3a_n(t - \Delta t) + \frac{3}{2} a_n(t - 2\Delta t) - \frac{1}{3} a_n(t - 3\Delta t) \right]. \tag{37}$$

As for η_{xt}, the terms $a_{n,xt}$ are then computed from the terms $a_{n,t}$ using again a centered 5-node FD scheme in space.

3. Verification for regular nonlinear waves in uniform water depth

In this section, we demonstrate the accuracy of the proposed formulas for computing wave kinematics of a highly nonlinear periodic wave propagating with permanent form in uniform water depth. For a quantitative assessment, the numerical solution of SF theory is considered, which provides a solution of arbitrarily high accuracy for this case. The SF solution is obtained here by imposing that the mean Eulerian flow velocity at any point below the wave trough is null.

Given the still water depth h, wavelength L (or, equivalently, wave number $k = 2\pi/L$), and wave height H, a regular wave condition is defined. Here, we choose a challenging case: (i) the relative water depth is set to $h/L = 1$ (i.e. $kh = 2\pi$), achieving twice the traditionally accepted 'deep water' threshold ($kh = \pi$); (ii) a very high value of the wave

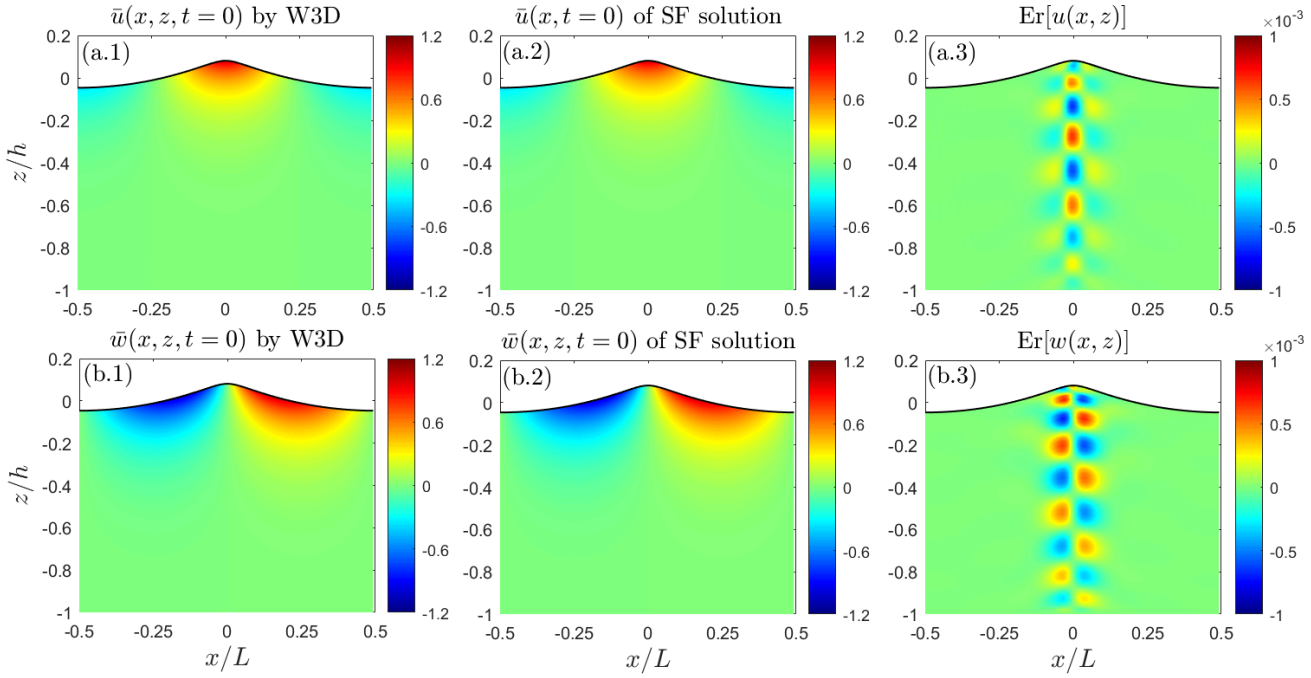

Figure 1: Normalized velocity fields $(\bar{u}, \bar{w})$ at $t = 0$ predicted by the W3D model in panels (a.1) and (b.1) and the corresponding SF solution in panels (a.2) and (b.2), respectively, and the relative error of the velocities obtained with two methods in panels (a.3) and (b.3). In each panel, the wave profile is outlined with a thick black line on the free surface.

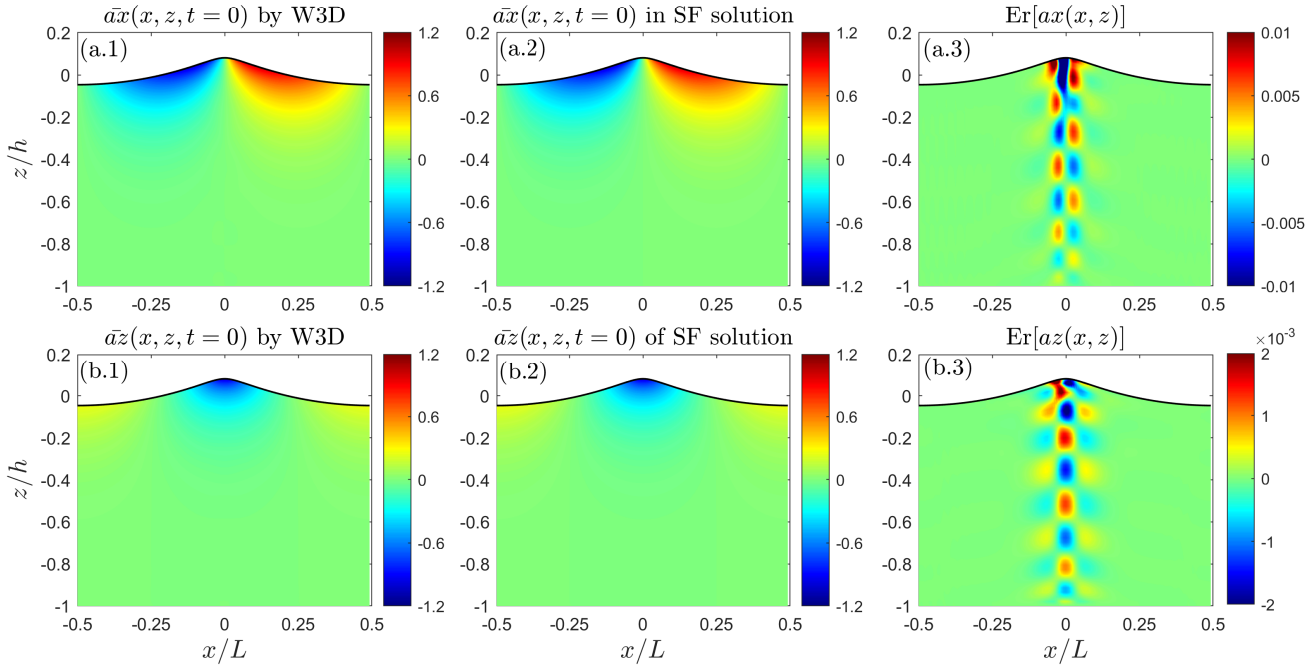

Figure 2: Normalized acceleration fields $(\bar{a}\bar{x}, \bar{a}\bar{z})$ at $t = 0$ predicted by the W3D model in panels (a.1) and (b.1) and the corresponding SF solution in panels (a.2) and (b.2), respectively, and the relative error of the accelerations obtained with two methods in panels (a.3) and (b.3). In each panel, the wave profile is outlined with a thick black line on the free surface.

steepness is selected $H/L = 12.73\%$ (i.e. $kH/2 = 0.40$). According to the approximate relationship giving the maximum stable wave height, expressed as eq. (32) of Fenton (1990), such a wave steepness represents 90% of the maximum wave height for the chosen relative water depth. In practice, the wavelength is set as $L = 64$ m. We use 25 Fourier coefficients for the expansion of the SF, providing a converged solution.

The spatial profiles of FSE (η) and free surface potential ($\tilde{\phi}$) computed with the SF method are given as initial

conditions to the W3D simulation. We run the W3D simulation over a periodic domain covering one wavelength exactly, which is discretized with 128 cells of constant size $\Delta x = L/128 = 0.5$ m. The theoretical wave period obtained from the SF solution is $T_{\rm SF} \equiv 2\pi/\omega_{\rm SF} \approx 5.916$ s. We note that, as expected, this period is shorter than the period obtained from the dispersion relation of linear waves:

$$T_{\rm lin} = \frac{2\pi}{\omega_{\rm lin}} = \frac{2\pi}{\sqrt{gk\tanh(kh)}} \approx 6.402\,\text{s}. \tag{38}$$

We note $T_{\rm SF}$ is smaller than $T_{\rm lin}$ because the SF wave solution follows a nonlinear dispersion relation which predicts a faster wave phase speed for a wave with the same wavelength in comparison to the prediction of linear dispersion. In the simulation, a constant time step $\Delta t = T_{\rm SF}/128 \approx 0.046$ s is chosen, which results in a Courant–Friedrichs–Lewy number CFL $\equiv (L\Delta t)/(T_{\rm SF}\Delta x) = 1$. Initial conditions for $(\eta(x), \tilde{\phi}(x))$ at $t = -3\Delta t$ from the SF solution are provided as input to W3D, and time integration is performed over $3\Delta t$ to reach $t = 0$ s where results are compared with the SF solution. As kh is quite large here and waves are strongly nonlinear, we choose $N_T = 11$ in the W3D simulation after calibration.

The computed velocities and accelerations are presented hereafter in a dimensionless way, normalized with the modulus of the corresponding quantities expressed from linear wave theory (under the same condition (h, L, H) as for the SF solution) at mean water level (i.e., $z = 0$), that is $\bar{u} \equiv u/U_{\rm lin}, \bar{w} \equiv w/W_{\rm lin}, \bar{ax} \equiv ax/Ax_{\rm lin}, \bar{az} \equiv az/Az_{\rm lin}$, with:

$$U_{\rm lin} = gka_{\rm lin}/\omega_{\rm lin} \tag{39}$$

$$W_{\rm lin} = a_{\rm lin}\omega_{\rm lin} \tag{40}$$

$$Ax_{\rm lin} = gka_{\rm lin} \tag{41}$$

$$Az_{\rm lin} = a_{\rm lin}\omega_{\rm lin}^2 \tag{42}$$

with $a_{\rm lin} \equiv H/2$. The relative errors are made dimensionless by the maximum value of the modulus of the SF solution, e.g. for the vertical velocity component:

$$\text{Er}[w(x,z)] = \frac{w_{\rm W3D}(x,z) - w_{\rm SF}(x,z)}{|w_{\rm SF}(x, z=\eta)|_{\max}}. \tag{43}$$

The non-dimensional velocity fields ($\bar{u}$ and $\bar{w}$) at $t = 0$ (with wave crest at $x = 0$) in both W3D simulation and SF theory are displayed in Fig. 1, with their relative errors provided. As shown in Fig. 1(a.1–a.2) and (b.1–b.2), the velocity fields $(\bar{u}, \bar{w})$ are well predicted by the W3D model, with the coloured maps of theoretical and simulated velocity components being visually indistinguishable from each other. The plots (a.3–b.3) of relative error show the differences appear mainly below the wave crest and remain less than 0.1% all over the water column. The velocity field underneath the wave trough is well predicted, with the maximum relative error below 10^{-4}.

The acceleration at $t = 0$ is also computed, which involves the backward FD scheme (37) to evaluate the time derivative of the coefficients $a_n(x, t = 0)$. Fig. 2 shows the non-dimensional acceleration fields ($\bar{ax}$ and $\bar{az}$) at $t = 0$ in both W3D simulation and SF theory, as well as the relative error between them. Again, the simulated and theoretical acceleration (x, z)-maps are visually identical in the current colour scale of panels (a.1–a.2) and (b.1–b.2) in Fig. 2. The relative error of ax in panel (a.3) achieves the most prominent values beneath the wave crest. It is larger than the ones reached for the velocity components but remains bounded by 1%. The relative error is lower for the vertical acceleration az in panel (b.3), not exceeding 0.5%. These low error levels confirm the accuracy of the scheme chosen to evaluate $a_{n,t}$, bearing in mind that the model has evolved the input initial solution for 3 time-steps to reach the state shown in Fig. 2.

In conclusion, the W3D schemes can model with accuracy the wave kinematics beneath highly nonlinear (close-to-breaking) regular waves, without any sign of singularity. Larger errors are observed below the wave crest (never exceeding 0.1% for the velocity components and 1% for the acceleration components in the case shown here). It is also observed that the relative errors of the horizontal components of velocity and acceleration are a bit higher than those of their vertical counterparts.

4. Experimental validation for regular nonlinear waves in variable water depth

4.1. Experimental configuration

In this section, W3D's performance is evaluated by simulating an experimental test for which detailed measurements of the FSE and orbital velocity beneath regular waves are available. We chose a case with regular nonlinear waves propagating over an inhomogeneous medium performed at the hydrodynamics laboratory of the Department of Mathematics of the University of Oslo (Norway) and introduced in Lawrence et al. (2021a). The wave flume is 24.6 m long and 0.5 m wide. A trapezoidal-shaped bar was installed on the bottom, consisting of plane ascending and descending slopes with 1/3.81 gradient and 1.6 m length each, and a plateau of 1.6 m length that connects the two slopes. The water depth is changed from $h_1 = 0.53$ m before and after the bar to $h_2 = 0.11$ m atop the bar, so that the height of the bar above the horizontal seabed is 0.42 m (see Fig. 3). A piston-type wavemaker is located at one end of the flume, and a wave absorbing zone at the other. Given the origin of the x-axis set at the beginning of the bar crest, the abscissa of the wavemaker is -12.36 m.

The measuring devices contain four ultrasonic wave probes to record the FSE, and one Nortek "Vectrino" acoustic Doppler velocimeter (ADV) to record the velocity at an elevation $z_0 = -0.05$ m below the SWL, giving $z_0 \approx -0.1h_1 \approx -0.45h_2$. The test with regular waves presented in Section 3.4 of Lawrence et al. (2021a) is considered here. In this test, the wave frequency is set as $f_0 = 0.7$ Hz (i.e., $T_0 \approx 1.43$ s, the corresponding wavelength before the bar is $L_1 = 2\pi/k_1 = 2.69$ m according to the linear wave dispersion relation) and the wave amplitude $H_0 = 2a_0 = 0.0270$ m. In such a configuration, the incident wave steepness is $\epsilon_1 \equiv k_1 a_0 =$

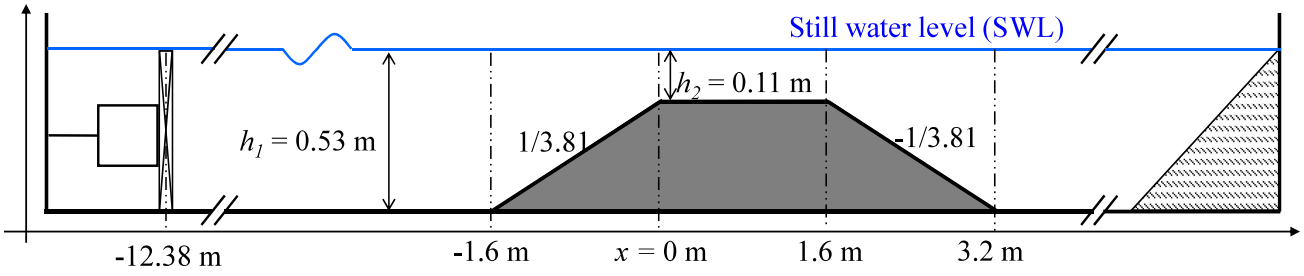

Figure 3: Sketch of the bathymetry used in the experiments reported in Lawrence et al. (2021a)

0.032 (or $H_0/h_1 = 0.051$) and the relative water depth $\mu_1 \equiv k_1 h_1 = 1.237$ (or $h_1/L_1 = 0.197$), resulting in an Ursell number $\mathrm{Ur}_1 \equiv \left(H_0/h_1\right)\left(L_1/h_1\right)^2 = 13.12$. Over the bar, the parameters are then $\epsilon_2 = 0.059$ (or $H_0/h_2 = 0.246$), $\mu_2 = 0.483$ (or $h_2/L_2 = 0.077$) and $\mathrm{Ur}_2 = 414.93 > 100$. Therefore the relative importance of nonlinearity is considerably enhanced by the shoal. The wave field near the wavemaker is of intermediate nonlinearity, yet it results in highly nonlinear but non-breaking waves over the bar. The same configuration was tested 31 times, such that the FSE was measured at 124 positions and the horizontal velocity at 31 positions. The measurements were performed in a sufficiently short time to avoid the effects of reflection at the end of the flume.

4.2. Numerical model setup

In the numerical flume, the waves are generated and damped within two relaxation zones of 8 m in length (approximately $3L_1$) located at both ends of the numerical flume. The effective computation domain for wave propagation (i.e., excluding the two relaxation areas) starts at $x = -5.5$ m and ends at $x = 10.3$ m. The governing equations are discretized with constant space and time step, $\Delta x = 0.04$ m and $\Delta t = 0.02$ s, respectively. Such a choice results in CFL= 0.94 in the deeper flat regions and CFL= 0.50 over the bar crest. The polynomial order is set to $N_T = 7$.

4.3. Free surface elevation

Comparisons of the measured and computed FSE time profiles are shown in Fig. 4 at 6 positions over a time window of $3T_0$. Before the bar (probes #1 and #25), the waves are nearly symmetric in both the horizontal and vertical directions. As waves propagate over the bar (probes #70 and #106), the wave profiles become asymmetric, and secondary crests manifest. These secondary crests are related to the development of high-order harmonics that propagate with a different velocity in comparison to the carrier wave. As waves propagate over the de-shoaling slope (probes #115 and #124), due to the presence of bound and free superharmonics (propagating with different velocities) the free surface time profile is very variable from one position to another. It should be noticed that after the de-shoaling slope (probe #124), the wave profile is asymmetric, with sharper troughs and flatter crests. The evolution of the wave profile along the flume is very well reproduced by the model, despite some slight phase shifts at probes #115 and #124.

To better illustrate the evolution of the waves over the varying bathymetry and to assess the magnitude of nonlinear effects, a Fourier analysis is applied to both the measured and simulated time series. Fig. 5(a) shows the spatial evolution of the amplitudes of the first six harmonics (i.e. wave components with frequencies nf_0, with $n = 1, ..., 6$), normalized by the amplitude measured at probe #1, denoted as a_0. The fourth to sixth harmonics are duplicated in Fig. 5(b) with a reduced range in y-axis to have a better view. The evolution of the primary component shows some oscillations before and over the bar, this is expected to be the result of reflection (by both the ascending and descending slopes). Over the bar crest, the amplitude of the primary component starts to decrease due to the enhancement of the amplitudes of the high-order super-harmonics. The second harmonic is considerably increased over the bar crest and remains on a high level. Eventually, the amplitude of this second harmonic becomes comparable to the primary component over the de-shoaling slope. The third harmonic is also increased over the bar with some oscillations, and it decreases over the de-shoaling slope. The evolution trends of the first three harmonics are very closely reproduced by the model. In Fig. 5(b), the evolution trend of the fourth to sixth harmonics is similar to that of the third harmonics and is also well captured by the model. It is seen that measured results scatter around the simulated results, this could be explained by the fact that the fourth to sixth harmonics are of small magnitudes and may be influenced by noise during the measurements.

As shown in Fig. 4, waves become asymmetric in both vertical and horizontal directions when propagating over the submerged bar. The magnitudes of the vertical and horizontal asymmetry are measured by the skewness of the FSE and its Hilbert transform (Elgar and Guza, 1985), $\lambda_3(\eta)$ and $\lambda_3(\mathcal{H}(\eta))$ (known as asymmetry parameter, with $\mathcal{H}$ denoting the Hilbert transform operator), respectively. The kurtosis is a measure of the extreme values in a time series: for irregular waves, it is related to the occurrence probability of freak waves, and for regular waves, it is still an important index that characterizes wave nonlinearity. For a normalized random variable $\bar{X}$ with a zero mean and a unit variance, the skewness, asymmetry and kurtosis parameters are defined respectively as:

$$\lambda_3(\bar{X}) = \left\langle \bar{X}^3 \right\rangle, \tag{44}$$

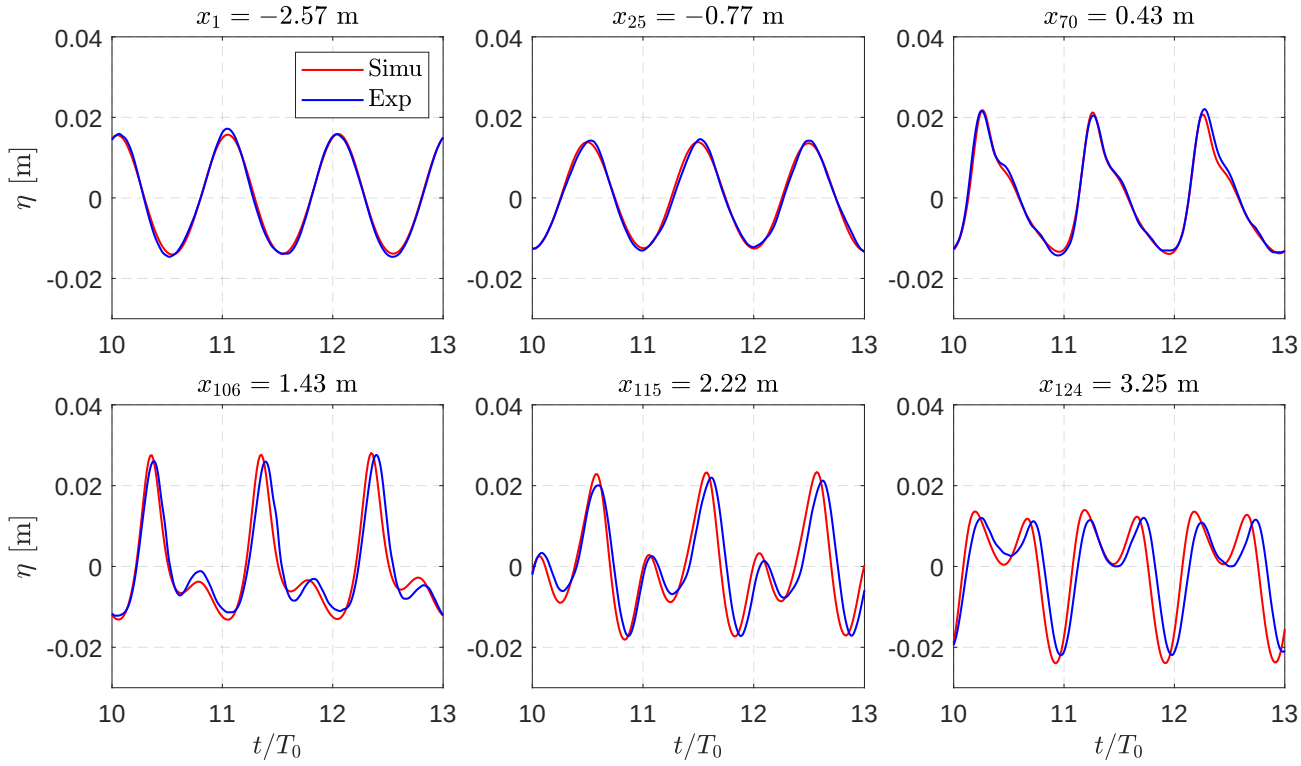

Figure 4: Comparison of measured and computed FSE temporal profiles at 6 locations for the nonlinear regular wave experiment of Lawrence et al. (2021a)

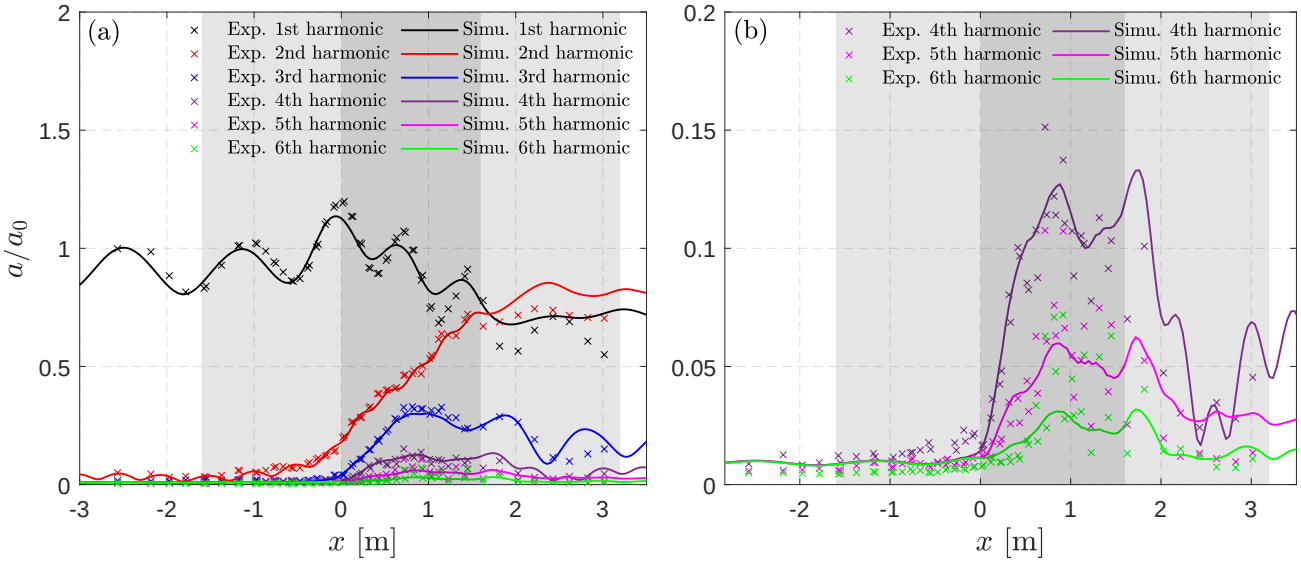

Figure 5: (a) Spatial evolution of measured and computed normalized amplitudes of the first 6 harmonics of the FSE for the nonlinear regular wave experiment of Lawrence et al. (2021a). (b) Close-up view of the fourth to sixth harmonics, with a reduced extent of the vertical axis. The gray areas indicate the extent of the submerged bar.

$$\lambda_3[\mathcal{H}(\bar{X})] = \left\langle \mathcal{H}(\bar{X})^3 \right\rangle, \tag{45}$$

$$\lambda_4(\bar{X}) = \left\langle \bar{X}^4 \right\rangle. \tag{46}$$

where $\langle\cdot\rangle$ denotes a mean operator, $\bar{X}$ could be normalized FSE, velocity or acceleration. In this subsection, we take $\bar{X}$ as $\bar{\eta}$. As we are discussing regular waves, in practice, the skewness, asymmetry and kurtosis are computed for the averaged free surface profile over one wave period. In the linear framework, the skewness and asymmetry of a sinusoidal wave over one (or multiple) period(s) are 0, while the kurtosis is expected to be 1.5. The deviation of these parameters from their linear expectation is an indication of the magni-

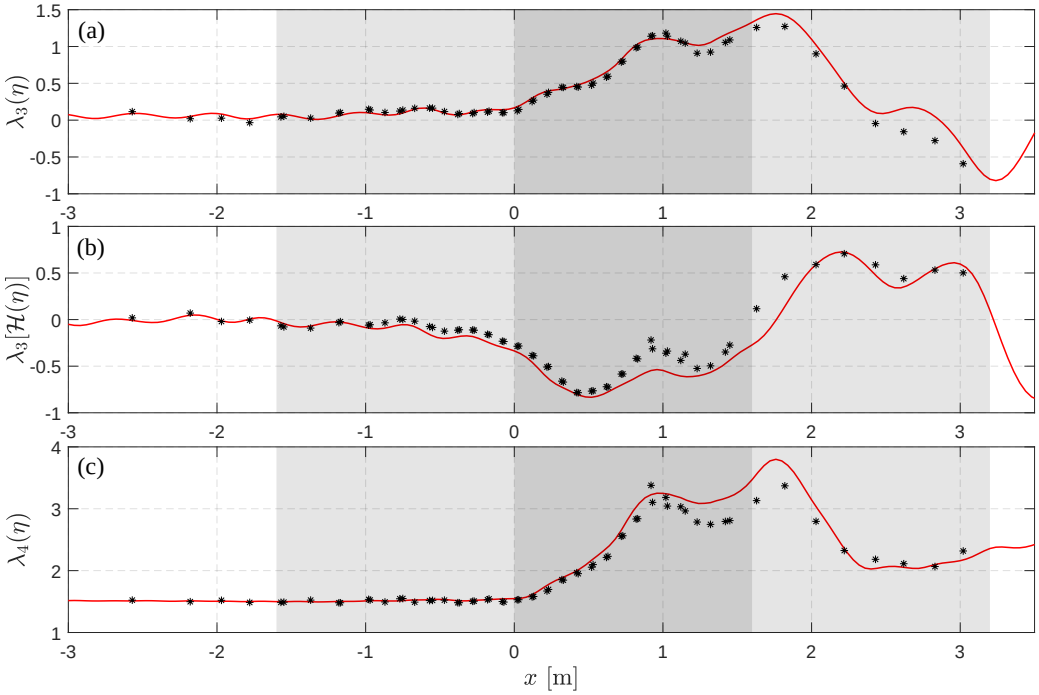

Figure 6: Spatial evolution of statistical moments of the measured and computed FSE for the nonlinear regular wave experiment of Lawrence et al. (2021a). The gray areas indicate the extent of the submerged bar.

tude of nonlinearity.

The evolution of skewness, asymmetry and kurtosis is shown in Fig. 6. It is observed that in Fig. 6(a), the skewness is increased over the bar crest, indicating waves with sharper crests and flatter troughs. It is then significantly decreased over the de-shoaling area, indicating that deep troughs and smaller crests develop in the wave profile in this area. In Fig. 6(b), the evolution of the asymmetry parameter indicates that the wave profile first leans forward then backward, and eventually restores a symmetric shape in the horizontal direction. Symmetrical wave profiles in both horizontal and vertical directions are not recovered after the de-shoaling zone, at least within the current spatial scale. In Fig. 6(c), the kurtosis of FSE shows a similar evolution trend as the skewness, it starts to deviate from the linear expectation 1.5 after the up-slope and increases significantly over the bar crest. Eventually, the kurtosis does not recover 1.5 after passing over the down-slope, and remains higher than this linear expectation instead.

4.4. Orbital wave velocities at $z_0 = -0.05$ m

Fig. 7 shows the evolution profiles of $u(z_0)$ ($z_0 = -0.05$ m) at the same six positions as in Fig. 4, within again a time frame of $3T_0$. In general, the evolution of $u(z_0)$ profile is quite similar to that of η. The main difference between the evolution of $u(z_0)$ and η is that the contribution of the high-order harmonics is enhanced in the time series of $u(z_0)$. The enhancement is proportional to the wave number of high-order harmonics, and this explains the more pronounced secondary peaks over and after the submerged bar (at locations of probes #29 and #30 for instance).

The harmonic analysis is performed for both the measured and computed horizontal velocity $u(z_0)$. It is shown in Fig. 8(a) that the magnitudes and the evolution trends of $u(z_0)$ are reproduced by the model with high accuracy to the third order. In Fig. 8(b), the measured fourth to sixth-order harmonics of $u(z_0)$ are slightly lower than the model predictions. Again, the measured fourth to sixth harmonics show some oscillations around their mean levels, which could be related to digital noise. The spatial evolution of skewness, asymmetry and kurtosis is displayed in Fig. 9. The evolution trends of these statistical parameters of $u(z_0)$, in particular the skewness and asymmetry parameters, are very similar to those of η, indicating that the shapes of the horizontal velocity and FSE profiles evolve similarly.

To sum up, the various comparisons confirm the high accuracy of the W3D model in computing the horizontal velocity beneath nonlinear waves. In contrast, Lawrence et al. (2021a) indicate that they had to use two different models to simulate this case, namely a HOS-type model to predict the FSE field and a variational Boussinesq model to calculate the velocities in the fluid domain.

4.5. Eulerian wave accelerations at $z_0 = -0.05$ m

The horizontal acceleration $ax(z_0) = (\partial u/\partial t)\,|_{z=z_0}$ is not directly available from the measurements. Here, it is estimated by computing the time derivative of the measured $u(z_0)$ signal, using a centered FD scheme over a stencil of 5 signal points (similar to eq. (36)). In the model, the acceleration is directly evaluated using eq. (25). For comparison, we also computed it by deriving the simulated $u(z_0)$ time series with respect to time, using the same FD scheme as for

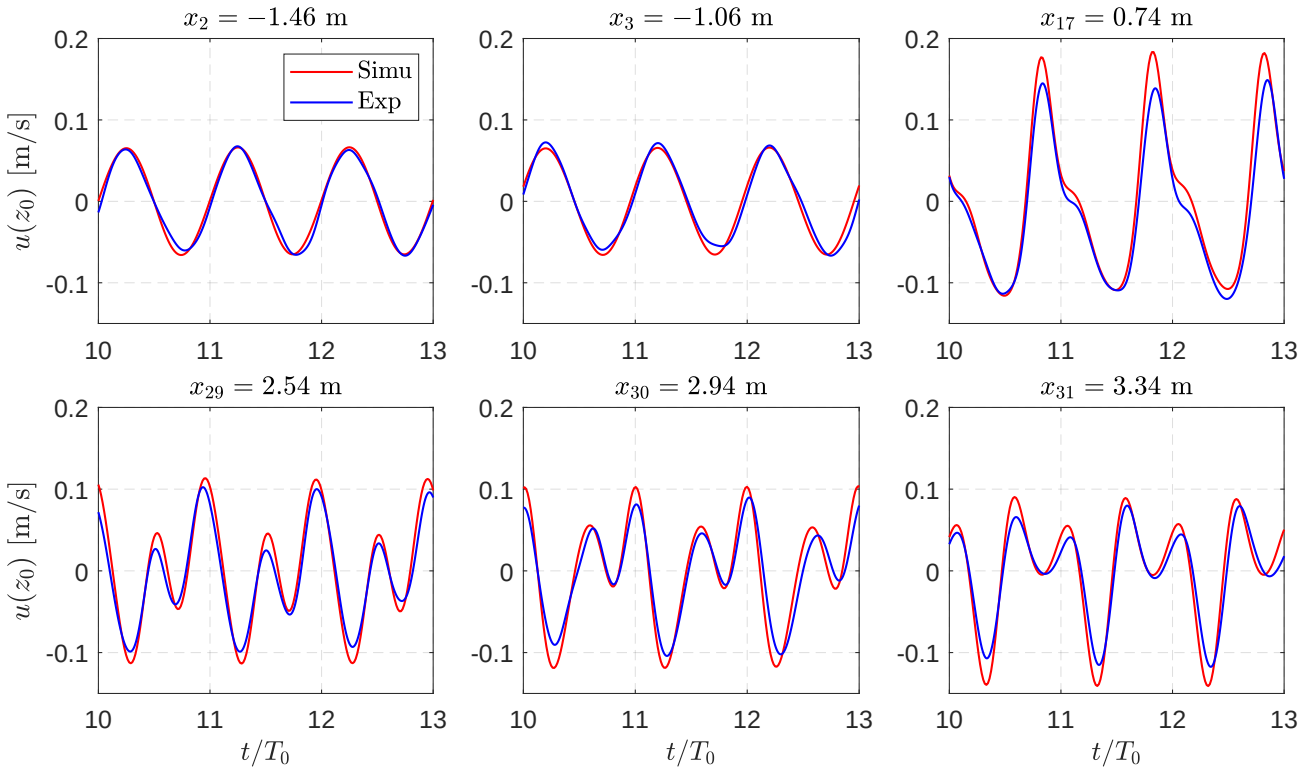

Figure 7: Comparison of measured and computed horizontal velocity $u(z_0)$ temporal profiles at 6 locations for the nonlinear regular wave experiment of Lawrence et al. (2021a).

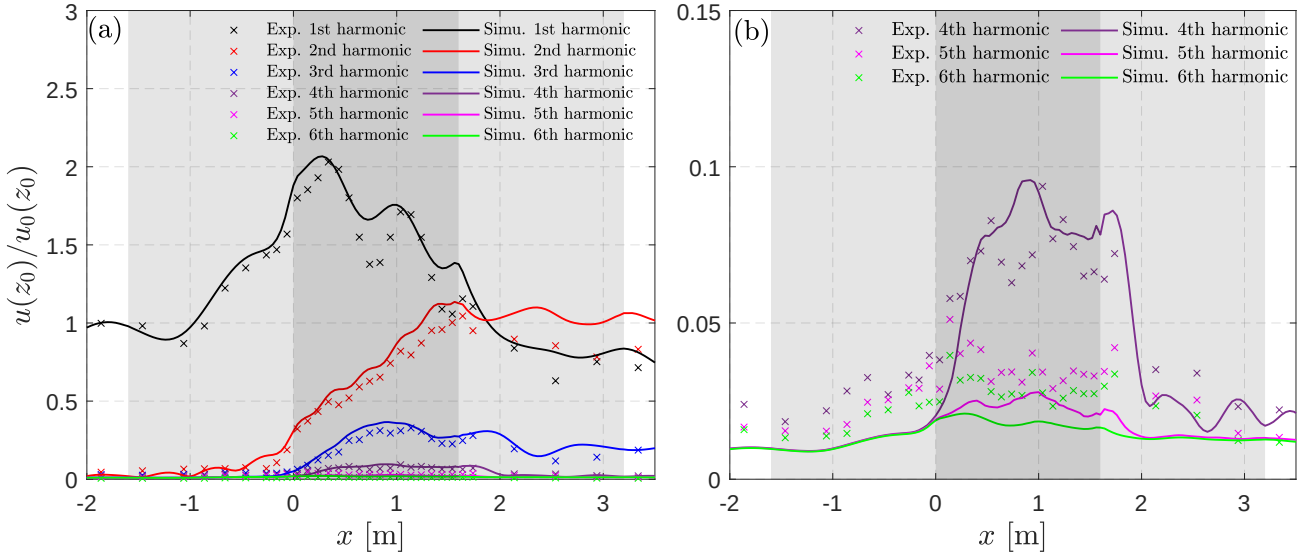

Figure 8: (a) Spatial evolution of normalized measured and computed amplitudes of the first 6 harmonics of the horizontal velocity $u(z_0)$ for the nonlinear regular wave experiment of Lawrence et al. (2021a). (b) Close-up view of the fourth to sixth harmonics, with a reduced extent of the vertical axis. The gray areas indicate the extent of the submerged bar.

the measurements.

In Fig. 10, the time profiles of $ax(z_0)$ at 6 locations (same as in Fig. 7) are shown. In each panel of Fig. 10, the time profiles of $ax(z_0)$ derived from the measured and simulated $u(z_0)$ with FD method, and simulated $ax(z_0)$ evaluated with eq. (25) are superimposed. It is seen that the $ax(z_0)$ directly computed with eq. (25) is in good agreement with that calculated from $u(z_0)$ with the FD method, thus validating our implementation of the acceleration computation. In the following, unless otherwise stated, simulated $ax(z_0)$ refers to the results obtained with eq. (25); measured $ax(z_0)$ refers to the acceleration evaluated from the measured $u(z_0)$ with the FD

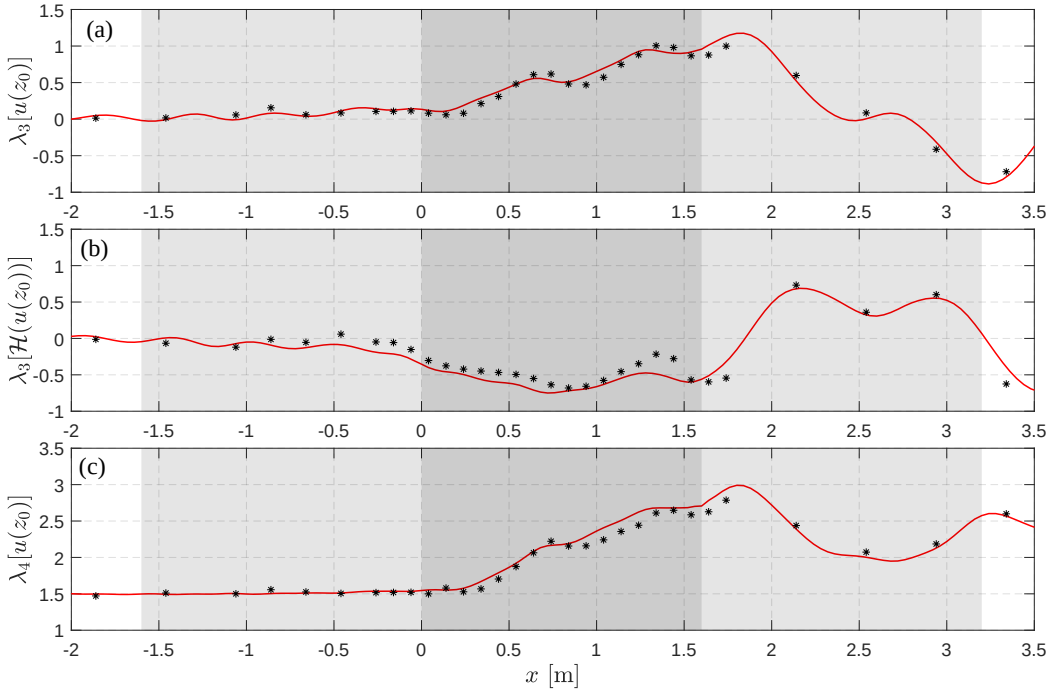

Figure 9: Spatial evolution of statistical moments of the measured and computed horizontal velocity $u(z_0)$ for the nonlinear regular wave experiment of Lawrence et al. (2021a). The gray areas indicate the extent of the submerged bar.

method. The agreement between the simulated and the measured $ax(z_0)$ is fairly good throughout the domain, although some differences in the magnitude of crests and troughs develop after the up-slope.

The harmonic analysis is performed for both the simulated and measured $ax(z_0)$ time series, with the evolution of the amplitudes of the first six harmonics displayed in Fig. 11. In Fig. 11(a), it is seen that the agreement between the simulated and measured results is reasonable. Yet, the second-order harmonic is overestimated in the simulation starting around $x = 0.5$ m, leading to higher crests and deeper troughs in the simulated $ax(z_0)$ time series. It is noted that the amplitudes of the super-harmonics (second and higher orders) are increasing when comparing the spectral evolution of η, $u(z_0)$, and $ax(z_0)$ in space. This is the result of the free super-harmonics excited by the shoal, which produce larger amplitudes of velocity and acceleration in comparison to the bound components.

In Fig. 12, the spatial evolution of skewness, asymmetry, and kurtosis of $ax(z_0)$ are shown. It is seen that the simulated results are in very good agreement with the measured results. The evolution trends of these parameters are evidently different from those for η and $u(z_0)$, especially after the up-slope: the local peak of the skewness appears much closer to the end of the up-slope, and the asymmetry parameter is positive over the bar. It is speculated that the differences are related to the phase differences between horizontal acceleration and horizontal velocity. The kurtosis increases rapidly after the shoal and remains at a high level over the bar and a short distance over the de-shoaling zone. The evolution trends of these parameters are in line with the indication of stronger second- and higher-order harmonics observed in Fig. 11. It is stressed that the kurtosis after de-shoal is hard to predict, and the W3D model performs well for that purpose, providing excellent prediction of not only the kurtosis of FSE but also of the kinematics underneath.

5. Conclusion

In this study, new formulations of the particle kinematics, namely orbital velocities and accelerations, have been developed in the FNPF wave model Whispers3D, which uses a basis of orthogonal Chebyshev polynomials of the first kind to project the vertical structure of the velocity potential. With the potential expressed (and approximated) in a polynomial form as given by eq. (8) where the main unknowns are then the a_n coefficients ($n = 0, 1, ..., N_T$), the expressions of particle kinematics could be derived explicitly. The estimation of horizontal and vertical velocities involves the spatial derivation of the potential in the corresponding direction, which can be obtained either analytically or with the FD method without additional information in the time domain. However, the estimation of particle accelerations involves the time derivative of the velocity components. In the model, this requires the computation of the time derivatives of a_n coefficients, which can be obtained by using either a backward (in time) FD scheme in the course of the simulation or a centered FD scheme after the completion of the run. The results shown here are obtained with a four-point backward FD scheme (i.e. using the value at the current time plus the ones at the three previous time steps). The accuracy and efficiency in the computation of the particle kinemat-

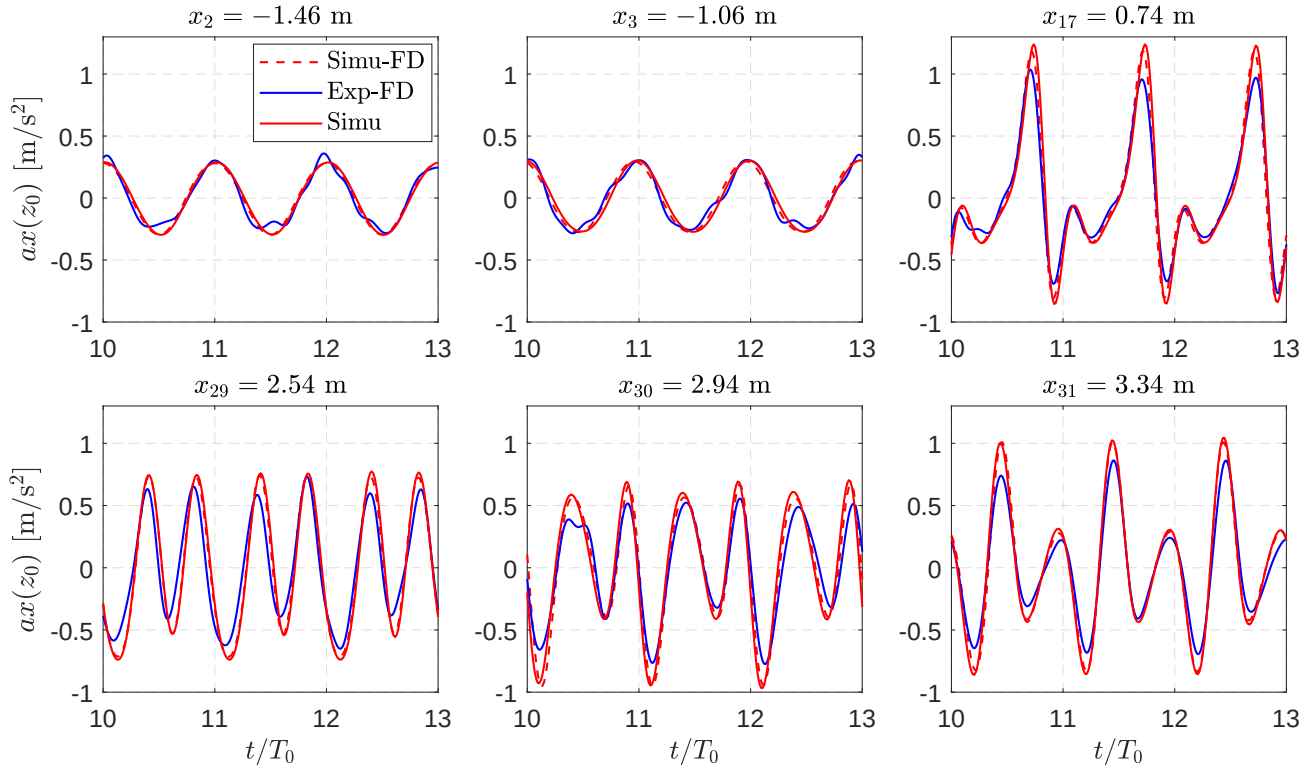

Figure 10: Comparison of the temporal profiles of the horizontal acceleration $ax(z_0)$, between the time-derivative of the measured horizontal velocity and the computed acceleration given by the model at 6 locations for the nonlinear regular wave experiment of Lawrence et al. (2021a).

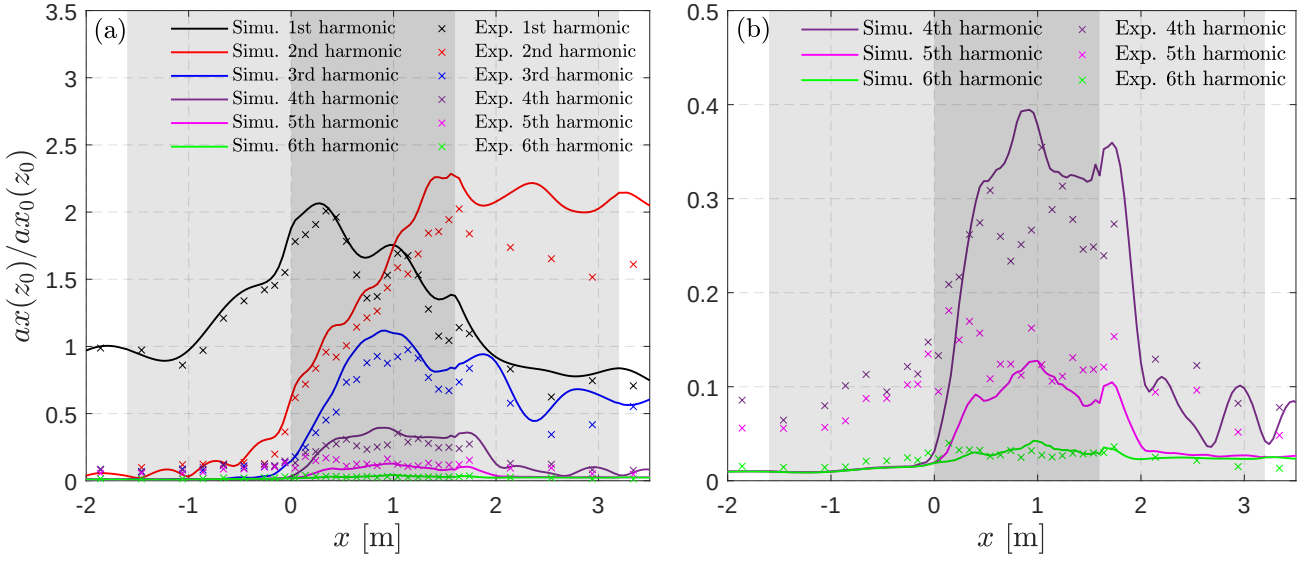

Figure 11: (a) Spatial evolution of normalized measured and computed amplitudes of the first 6 harmonics of the horizontal acceleration $ax(z_0) = u_t(z_0)$ for the nonlinear regular wave experiment of Lawrence et al. (2021a). (b) Close-up view of the fourth to sixth harmonics, with a reduced extent of the vertical axis. The gray areas indicate the extent of the submerged bar.

ics are governed by the maximum degree of the Chebyshev polynomial N_T in eq. (8).

We have then demonstrated the capability and accuracy of the model to simulate kinematics beneath regular nonlinear wave trains in either uniform or variable water depth through comparisons with an analytical solution and experimental measurements. In the case of regular waves propagating over a flat bottom, a deep-water ($kh = 2\pi$) and nearly-breaking ($ka = 0.40$) wave condition is tested. With $(\eta, \tilde{\phi})$ calculated from the SF theory and imposed as initial condi-

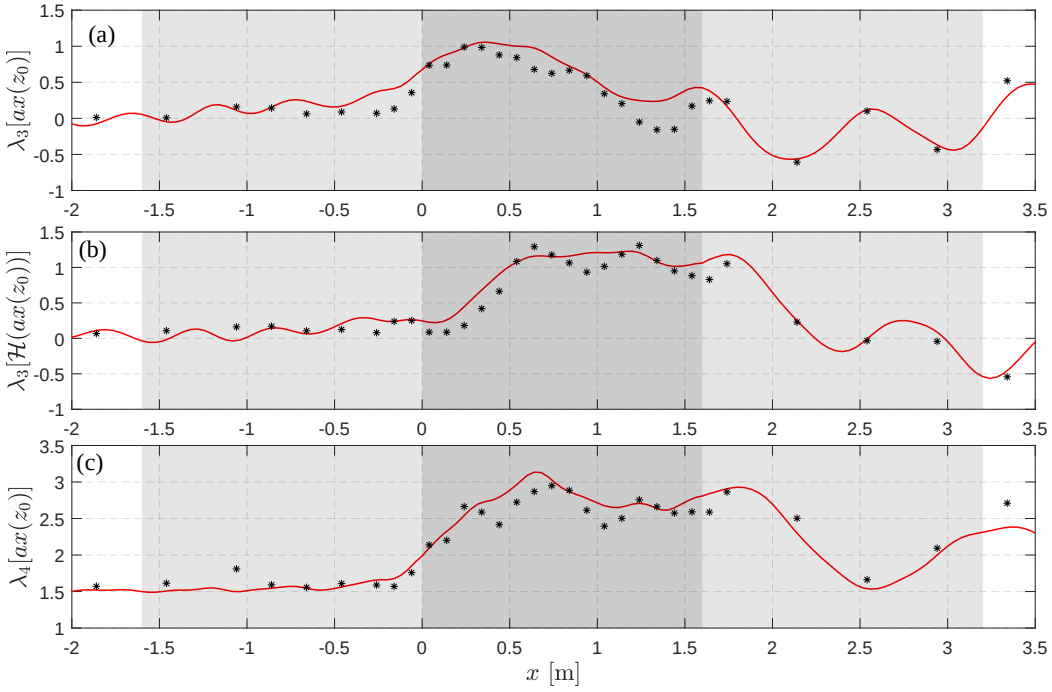

Figure 12: Spatial evolution of statistical moments of the measured and computed horizontal acceleration $ax(z_0) = u_t(z_0)$ for the nonlinear regular wave experiment of Lawrence et al. (2021a). The gray areas indicate the extent of the submerged bar.

tions on the free surface, the W3D model successfully computes the kinematics in the whole fluid domain beneath the free surface. The errors of computed FSE, velocities, and accelerations in comparison to the reference SF solution occur mainly beneath the wave crest, yet remain very low (below 0.1% for velocities and 1% for the accelerations) with $N_T = 11$. An even better agreement could be achieved with a further increase of N_T, at the cost of an additional computational burden though. In the case of regular waves propagating over an uneven bottom (submerged trapezoidal bar), the experimental test reported in Lawrence et al. (2021b) is reproduced with the W3D model. A Fourier analysis of both measured and simulated times series shows a very good to excellent agreement between simulated results and measurements achieved for the amplitudes up to the sixth-order super-harmonics of FSE, velocities, and accelerations. The spatial evolution trends of statistical parameters describing wave nonlinearity of the kinematics (skewness, asymmetry, kurtosis) are also very well described by the model.

As a general conclusion, the W3D model is capable of computing the kinematics beneath strongly nonlinear waves very accurately under the framework of potential wave theory. In comparison to other existing models, some advantages of the W3D model can be summarized as follows:

1. It is a single-layer model that can handle nonlinear waves in a broad range of relative water depth, whereas a multi-layer approach is often required for higher-order Boussinesq-type models aiming at a similar range of application (see e.g. Liu and Fang, 2016; Fang et al., 2022);
2. With the newly developed compact formulas, namely eqs. (17)–(18) for the velocity components and eqs. (25)–(26) for the acceleration components, explicit high-order polynomial expressions are available to compute the wave-induced kinematics at any point at or below the free surface.
3. The model is free from any singularity issue when computing the kinematics throughout the water column, which is different from other approaches as the BEM for instance, in which singularities appear for nodes located at the free surface (see e.g. Lafe et al., 1980; Wang and Tsay, 2005).
4. It can describe kinematics beneath strongly nonlinear waves with high accuracy. In contrast, tackling the same question with the HOS modelling framework can be of larger error close to the free surface, as observed by Lawrence et al. (2021a) for instance, who had to rely on a two-model approach, namely a HOS model for simulating the wave field evolution and a variational Boussinesq model to subsequently compute wave kinematics.

In the companion Part II article (Zhang et al., 2024), we provide additional validation of the numerical model against irregular wave experiments performed by Trulsen et al. (2020) in which the same bottom profile as in section 4 was adopted. The combination of measured and numerically simulated long time-series of wave kinematics permits studying the statistical distributions of particle velocities and accelerations, and proposing and validating a new statistical model of log-normal type for these kinematics variables.

CRediT authorship contribution statement

Michel Benoit: Writing – Review & Editing, Writing – Original Draft, Supervision, Methodology, Conceptualization. **Jie Zhang:** Writing – Original Draft, Investigation, Funding acquisition, Formal analysis. **Yuxiang Ma:** Resources, Writing – Review & Editing, Supervision.

Declaration of competing interest

The authors declare that they have no known competing financial interests or personal relationships that could have appeared to influence the work reported in this paper.

Acknowledgments

This work was supported by the National Natural Science Foundation of China (Grant No. 52101301), and the China Postdoctoral Science Foundation (Grants No. 2023T160078, 2021M690523). The authors would like to express their gratitude to Christopher Lawrence, Karsten Trulsen, and Odin Gramstad for kindly sharing their experimental dataset in Lawrence et al. (2021a).

References

Aggarwal, A., Chella, M.A., Kamath, A., Bihs, H., Arntsen, Ø.A., 2016. Irregular wave forces on a large vertical circular cylinder. Energy Procedia 94, 504–516. doi:10.1016/j.egypro.2016.09.223.

Antuono, M., Colagrossi, A., Marrone, S., Lugni, C., 2011. Propagation of gravity waves through an SPH scheme with numerical diffusive terms. Compt. Phys. Commun. 182, 866–877. doi:10.1016/j.cpc.2010.12.012.

Bassi, C., Bonaventura, L., Busto, S., Dumbser, M., 2020. A hyperbolic reformulation of the Serre-Green-Naghdi model for general bottom topographies. Comput. Fluids 212, 104716. doi:10.1016/j.compfluid.2020.104716.

Belibassakis, K.A., Athanassoulis, G.A., 2011. A coupled-mode system with application to nonlinear water waves propagating in finite water depth and in variable bathymetry regions. Coast. Eng. 58, 337–350. doi:10.1016/j.coastaleng.2010.11.007.

Benoit, M., Raoult, C., Yates, M.L., 2017. Analysis of the linear version of a highly dispersive potential water wave model using a spectral approach in the vertical. Wave Motion 74, 159–181. doi:10.1016/j.wavemoti.2017.07.002.

Berkhoff, J., 1972. Mathematical models for simple harmonic linear water waves: wave diffraction and refraction. Coast. Eng. Proc. (ICCE'1972) 1(13), 23. doi:10.9753/icce.v13.23.

Bingham, H.B., Madsen, P.A., Fuhrman, D.R., 2009. Velocity potential formulations of highly accurate Boussinesq-type models. Coast. Eng. 56, 467–478. doi:10.1016/j.coastaleng.2008.10.012.

Boussinesq, J., 1872. Théorie des ondes et des remous qui se propagent le long d'un canal rectangulaire horizontal, en communiquant au liquide contenu dans ce canal des vitesses sensiblement pareilles de la surface au fond. J. Math. Pures Appl. 17, 55–108.

Craig, W., Sulem, C., 1993. Numerical simulation of gravity waves. J. Comput. Phys. 108, 73–83. doi:10.1006/jcph.1993.1164.

Dalrymple, R.A., Rogers, B.D., 2006. Numerical modeling of water waves with the SPH method. Coast. Eng. 53, 141–147. doi:10.1016/j.coastaleng.2005.10.004.

Decorte, G., Toffoli, A., Lombaert, G., Monbaliu, J., 2021. On the use of a domain decomposition strategy in obtaining response statistics in non-Gaussian seas. Fluids 6, 28. doi:10.3390/fluids6010028.

Deng, Y., Zhu, C., Wang, Z., 2023. A comparative study of wave kinematics and inline forces on vertical cylinders under Draupner-type freak waves. Ocean Eng. 288, 115959. doi:10.1016/j.oceaneng.2023.115959.

Didenkulova, E., Didenkulova, I., Medvedev, I., 2023. Freak wave events in 2005–2021: statistics and analysis of favourable wave and wind conditions. Nat. Hazards Earth Syst. Sci. 23, 1653–1663. doi:10.5194/nhess-23-1653-2023.

Didenkulova, E.G., Pelinovsky, E.N., 2020. Freak waves in 2011–2018. Dokl. Earth Sci. 491, 187–190. doi:10.1134/s1028334x20030046.

Didenkulova, I., Pelinovsky, E., 2016. On shallow water rogue wave formation in strongly inhomogeneous channels. J. Phys. A: Math. Theor. 49, 194001. doi:10.1088/1751-8113/49/19/194001.

Dommermuth, D., 2000. The initialization of nonlinear waves using an adjustment scheme. Wave Motion 32, 307–317. doi:10.1016/s0165-2125(00)00047-0.

Dysthe, K.B., 1979. Note on a modification to the nonlinear Schrödinger equation for application to deep water waves. Proc. R. Soc. A: Math. Phys. Eng. 369, 105–114. doi:10.1098/rspa.1979.0154.

Elfrink, B., Baldock, T., 2002. Hydrodynamics and sediment transport in the swash zone: a review and perspectives. Coast. Eng. 45, 149–167. doi:10.1016/s0378-3839(02)00032-7.

Elgar, S., Guza, R.T., 1985. Observations of bispectra of shoaling surface gravity waves. J. Fluid Mech. 161, 425–448. doi:10.1017/S0022112085003007.

Fang, K., Liu, Z., Wang, P., Wu, H., Sun, J., Yin, J., 2022. Modeling solitary wave propagation and transformation over complex bathymetries using a two-layer Boussinesq model. Ocean Eng. 265, 112549. doi:10.1016/j.oceaneng.2022.112549.

Fenton, J.D., 1990. The Sea - Vol. 9: Ocean Engineering Science, Part A. Wiley. chapter 1. Nonlinear wave theories. pp. 3–25.

Fochesato, C., Dias, F., 2006. A fast method for nonlinear three-dimensional free-surface waves. Proc. R. Soc. A: Math. Phys. Eng. 462, 2715–2735. doi:10.1098/rspa.2006.1706.

Fredsøe, J., Deigaard, R., 1992. Mechanics of Coastal Sediment Transport. Advanced Series on Ocean Engineering: Vol. 3. World Scientific. doi:10.1142/1546.

Freilich, M.H., Guza, R.T., 1984. Nonlinear effects on shoaling surface gravity waves. Philos. Trans. A: Math. Phys. Eng. Sci. 311, 1–41. doi:10.1098/rsta.1984.0019.

Gouin, M., Ducrozet, G., Ferrant, P., 2016. Development and validation of a non-linear spectral model for water waves over variable depth. Eur. J. Mech. B Fluids 57, 115–128. doi:10.1016/j.euromechflu.2015.12.004.

Green, A.E., Laws, N., Naghdi, P.M., 1974. On the theory of water waves. Proc. R. Soc. A: Math. Phys. Eng. 338, 43–55. doi:10.1098/rspa.1974.0072.

Grilli, S.T., Skourup, J., Svendsen, I.A., 1989. An efficient boundary element method for nonlinear water waves. Eng. Anal. Boundary Elem. 6, 97–107. doi:10.1016/0955-7997(89)90005-2.

Harris, J.C., Dombre, E., Benoit, M., Grilli, S.T., 2014. Fast integral equation methods for fully nonlinear water wave modeling, in: Proc. 24th Int. Ocean Polar Eng. Conf. (ISOPE'2014), Busan, Korea, 15-20 June 2014, pp. ISOPE–I–14–449.

Hasimoto, H., Ono, H., 1972. Nonlinear modulation of gravity waves. J. Phys. Soc. Japan 33, 805–811. doi:10.1143/JPSJ.33.805.

Higuera, P., Lara, J.L., Losada, I.J., 2013. Simulating coastal engineering processes with OpenFOAM®. Coast. Eng. 71, 119–134. doi:10.1016/j.coastaleng.2012.06.002.

Jacobsen, N.G., van Gent, M.R., Wolters, G., 2015. Numerical analysis of the interaction of irregular waves with two dimensional permeable coastal structures. Coast. Eng. 102, 13–29. doi:10.1016/j.coastaleng.2015.05.004.

Kriebel, D.L., 1998. Nonlinear wave interaction with a vertical circular cylinder: wave forces. Ocean Eng. 7, 597–605.

Lafe, O.E., Liu, P.L.F., Liggett, J.A., Cheng, A.H.D., Montes, J.S., 1980. Singularities in Darcy flow through porous media. J. Hydraul. Div. 106, 977–997. doi:10.1061/jyceaj.0005457.

Larsen, B.E., Fuhrman, D.T., Roenby, J., 2019. Performance of interFoam on the simulation of progressive waves. Coast. Eng. J. 61, 380–400. doi:10.1080/21664250.2019.1609713.

Lawrence, C., Gramstad, O., Trulsen, K., 2021a. Variational Boussinesq model for kinematics calculation of surface gravity waves over

bathymetry. Wave Motion 100, 102665. doi:10.1016/j.wavemoti.2020.102665.

Lawrence, C., Trulsen, K., Gramstad, O., 2021b. Statistical properties of wave kinematics in long-crested irregular waves propagating over non-uniform bathymetry. Phys. Fluids 33, 046601. doi:10.1063/5.0047643.

Li, Z., Tang, T., Li, Y., Draycott, S., van den Bremer, T.S., Adcock, T.A.A., 2023. Wave loads on ocean infrastructure increase as a result of waves passing over abrupt depth transitions. J. Ocean Eng. Mar. Energy 9, 309–317. doi:10.1007/s40722-022-00269-4.

Liu, Z., Fang, K., 2016. A new two-layer Boussinesq model for coastal waves from deep to shallow water: Derivation and analysis. Wave Motion 67, 1–14. doi:10.1016/j.wavemoti.2016.07.002.

Madsen, P.A., Fuhrman, D.R., Wang, B., 2006. A Boussinesq-type method for fully nonlinear waves interacting with a rapidly varying bathymetry. Coast. Eng. 53, 487–504. doi:10.1016/j.coastaleng.2005.11.002.

Madsen, P.A., Schäffer, H.A., 1998. Higher–order Boussinesq–type equations for surface gravity waves: derivation and analysis. Philos. Trans. Royal Soc. A 356, 3123–3181. doi:10.1098/rsta.1998.0309.

Papoutsellis, C.E., Yates, M.L., Simon, B., Benoit, M., 2019. Modelling of depth-induced wave breaking in a fully nonlinear free-surface potential flow model. Coast. Eng. 154, 103579. doi:10.1016/j.coastaleng.2019.103579.

Paulsen, B.T., Bredmose, H., Bingham, H.B., 2014. An efficient domain decomposition strategy for wave loads on surface piercing circular cylinders. Coast. Eng. 86, 57–76. doi:10.1016/j.coastaleng.2014.01.006.

Porter, D., 2003. The mild-slope equations. J. Fluid Mech. 494, 51–63. doi:10.1017/s0022112003005846.

Raoult, C., Benoit, M., Yates, M.L., 2016. Validation of a fully nonlinear and dispersive wave model with laboratory non-breaking experiments. Coast. Eng. 114, 194–207. doi:10.1016/j.coastaleng.2016.04.003.

Raoult, C., Benoit, M., Yates, M.L., 2019. Development and validation of a 3D RBF-spectral model for coastal wave simulation. J. Comp. Phys. 378, 278—-302. doi:10.1016/j.jcp.2018.11.002.

Shi, J., Feng, X., Toumi, R., Zhang, C., Hodges, K., Tao, A., Zhang, W., Zheng, J., 2024. Global increase in tropical cyclone ocean surface waves. Nat. Commun. 15, 174. doi:10.1038/s41467-023-43532-4.

Simon, B., Papoutsellis, C.E., Benoit, M., Yates, M.L., 2019. Comparing methods of modeling depth-induced breaking of irregular waves with a fully nonlinear potential flow approach. J. Ocean Eng. Mar. Energy 5, 365–383. doi:10.1007/s40722-019-00154-7.

Stansberg, C.T., Huse, E., Krokstad, J.R., Lehn, E., 1995. Experimental study of non-linear loads on vertical cylinders in steep random waves, in: Proc. 5th Int. Ocean Polar Eng. Conf. (ISOPE'1995), The Hague, The Netherlands, 11-16 June 1995, pp. ISOPE–I–95–013.

Tian, Y., Sato, S., 2008. A numerical model on the interaction between nearshore nonlinear waves and strong currents. Coast. Eng. J. 50, 369–395. doi:10.1142/s0578563408001879.

Trulsen, K., Raustøl, A., Jorde, S., Rye, L.B., 2020. Extreme wave statistics of long-crested irregular waves over a shoal. J. Fluid Mech. 882, R2. doi:10.1017/jfm.2019.861.

Vested, M.H., Carstensen, S., Christensen, E.D., 2020. Experimental study of wave kinematics and wave load distribution on a vertical circular cylinder. Coast. Eng. 157, 103660. doi:10.1016/j.coastaleng.2020.103660.

Wang, J., Tsay, T.K., 2005. Analytical evaluation and application of the singularities in boundary element method. Eng. Anal. Bound. Elem. 29, 241–256. doi:10.1016/j.enganabound.2004.12.008.

Wang, Z., Zou, Q., Reeve, D., 2009. Simulation of spilling breaking waves using a two phase flow CFD model. Comput. Fluids 38, 1995–2005. doi:10.1016/j.compfluid.2009.06.006.

Wilson, J.F., 2002. Dynamics of Offshore Structures. Wiley.

Yates, M.L., Benoit, M., 2015. Accuracy and efficiency of two numerical methods of solving the potential flow problem for highly nonlinear and dispersive water waves. Int. J. Numer. Meth. Fluids 77, 616–640. doi:10.1002/fld.3992.

Zakharov, V.E., 1968. Stability of periodic waves of finite amplitude on the surface of a deep fluid. J. Appl. Mech. Tech. Phys. 9, 190–194. doi:10.1007/bf00913182.

Zelt, J.A., Gudmestad, O.T., Skjelbreia, J.E., 1995. Fluid accelerations under irregular waves. Appl. Ocean Res. 17, 43–54. doi:10.1016/0141-1187(94)00019-j.

Zhang, J., Benoit, M., 2021. Wave–bottom interaction and extreme wave statistics due to shoaling and de-shoaling of irregular long-crested wave trains over steep seabed changes. J. Fluid Mech. 912, A28. doi:10.1017/jfm.2020.1125.

Zhang, J., Benoit, M., Ma, Y., 2022. Equilibration process of out-of-equilibrium sea-states induced by strong depth variation: Evolution of coastal wave spectrum and representative parameters. Coast. Eng. 174, 104099. doi:10.1016/j.coastaleng.2022.104099.

Zhang, J., Ma, Y., Benoit, M., 2024. Kinematics of nonlinear waves over variable bathymetry. Part II: Statistical distributions of orbital velocities and accelerations in irregular long-crested seas. Coast. Eng. 193, 104589.